METASURFACES

Resonant metasurfaces for generating complex quantum states

Tomás Santiago-Cruz[1,2], Sylvain D. Gennaro[3,4], Oleg Mitrofanov[3,5], Sadhvikas Addamane[3,4], John Reno[3,4], Igal Brener[3,4]*, Maria V. Chekhova[1,2]*

Quantum state engineering, the cornerstone of quantum photonic technologies, mainly relies on spontaneous parametric downconversion and four-wave mixing, where one or two pump photons spontaneously decay into a photon pair. Both of these nonlinear effects require momentum conservation for the participating photons, which strongly limits the versatility of the resulting quantum states. Nonlinear metasurfaces have subwavelength thickness and allow the relaxation of this constraint; when combined with resonances, they greatly expand the possibilities of quantum state engineering. Here, we generated entangled photons via spontaneous parametric downconversion in semiconductor metasurfaces with high–quality factor, quasi-bound state in the continuum resonances. By enhancing the quantum vacuum field, our metasurfaces boost the emission of nondegenerate entangled photons within multiple narrow resonance bands and over a wide spectral range. A single resonance or several resonances in the same sample, pumped at multiple wavelengths, can generate multifrequency quantum states, including cluster states. These features reveal metasurfaces as versatile sources of complex states for quantum information.

Optical quantum state engineering mainly relies on nonlinear optical effects such as spontaneous parametric downconversion (SPDC) or spontaneous four-wave mixing (SFWM). These effects have been used to create a vast variety of photonic quantum states, including single (*1*) and entangled (*2*) photons, squeezed states (*3*), and cluster states (*4*–*6*). However, both SPDC and SFWM in conventional nonlinear crystals and waveguides require strict momentum conservation for the involved photons, which strongly limits the versatility of the states they produce. The emergent concept of quantum optical metasurfaces (QOMs) helps to overcome this constraint. Metasurfaces (i.e., arrays of nanoresonators) feature unique abilities to manipulate and control the amplitude, phase, and polarization of light in the nonlinear (*7*–*9*) and quantum (*10*, *11*) regimes using a single ultrathin device. In particular, all-dielectric metasurfaces made of materials with high second-order nonlinearities offer a potential route for on-chip quantum state generation (*12*–*14*). As a result of the subwavelength thickness of metasurfaces, the momentum conservation (or phase-matching) requirement is relaxed (*15*), enabling multiple nonlinear processes to occur with comparable efficiencies (*16*). In addition, optical resonances in metasurfaces and nanoresonators enhance the vacuum field fluctuations through enhanced density of states at certain wavelengths, boosting the spontaneous emission of photons (*17*).

[1]Max Planck Institute for the Science of Light, 91058 Erlangen, Germany. [2]Friedrich-Alexander-Universität Erlangen-Nürnberg, 91058 Erlangen, Germany. [3]Center for Integrated Nanotechnologies, Sandia National Laboratories, Albuquerque, NM 87185, USA. [4]Sandia National Laboratories, Albuquerque, NM 87185, USA. [5]University College London, London WC1E 7JE, UK.
*Corresponding author. Email: ibrener@sandia.gov (I.B.); maria.chekhova@mpl.mpg.de (M.V.C.)

Vacuum fluctuation enhancement scales with the quality (Q) factor of the resonance. In metasurfaces, Q-factors are especially high for bound states in the continuum (BIC) resonances (*18*, *19*), which are discrete-energy modes whose energy levels overlap with a continuous spectrum of radiating modes (*20*). In symmetry-protected BIC metasurfaces, the outcoupling of radiation in the normal direction is forbidden by symmetry (*19*). Hence, Q-factors of these modes may be infinite; in theory, they could infinitely enhance the spontaneous emission of photons and photon pairs. In practice, symmetry breaking (quasi-BICs) leads to finite enhancement (*19*), which can still be as high as 10^2 to 10^4.

Here, we report on the experimental generation of tunable photon pairs via SPDC driven by high-Q quasi-BIC resonances in gallium arsenide (GaAs) QOMs. Our QOMs emit frequency-degenerate and nondegenerate narrowband photon pairs tunable over more than 100 nm by changing either the optical pump or the spectral location of the resonances without appreciable loss of efficiency. Moreover, by judicious choice of resonance and pump wavelengths, we can simultaneously drive as many SPDC processes as necessary, obtaining frequency-multiplexed entangled photons and enabling multichannel heralding. Our work paves the way for building nanoscale sources of complex tunable entangled states for quantum networks.

In SPDC, a pump photon of a higher frequency ω_p downconverts in a second-order nonlinear material into a pair of signal and idler photons of lower frequencies, ω_s and ω_i, following energy conservation (Fig. 1A). Unlike in bulk crystals, SPDC in subwavelength sources does not require longitudinal momentum conservation (*15*), leading to the broadband emission of photon pairs over a wide range of angles (*21*, *22*). In optical nanoantennae and metasurfaces, however, the resonances select the range of wavelengths and wave vectors where the photon emission is enhanced (*12*, *14*, *23*). Therefore, with judicious choice and design of optical modes and resonances, metasurfaces can be used to generate tunable and unidirectional entangled photons.

To demonstrate SPDC with quasi-BICs, we fabricated various arrays of broken-symmetry resonators arranged in a square lattice of different periodicities and scaling by means of standard electron beam lithography and chlorine-based dry etching. Subsequent fabrication steps included epoxy bonding and curing, substrate lapping and polishing, wet etching, and transferring the metasurface onto a transparent fused silica substrate. We chose GaAs because it possesses one of the highest second-order susceptibilities among traditional materials, $\chi^{(2)}$ = 400 to 500 pm/V, for the range of pump wavelengths involved in this work; these susceptibilities exceed those of ferroelectric nonlinear materials such as lithium niobate by more than an order of magnitude (*24*). The structure of the metasurfaces is shown in Fig. 1B.

The existence of symmetry-protected BICs can be explained through symmetry breaking and coupling between allowed and forbidden optical Mie modes (*25*), or using group theory arguments (*26*). A metasurface consisting of square nanoresonators obeys C_2 and C_4 rotational symmetry; photons at the BIC frequency are trapped inside the resonators because of zero coupling to radiating modes. A small notch in the cube breaks the rotational symmetry (Fig. 1C) and transforms these symmetry-protected BICs into quasi-BICs, which can outcouple to the far field. Spectrally, they appear as narrow transmission peaks in the white-light far-field transmittance (Fig. 1D). The modes, labeled electric dipole (ED)–qBIC and magnetic dipole (MD)–qBIC, reach Q-factors of $Q_{BIC(ED)} \approx 330$ and $Q_{BIC(MD)} \approx 1000$, respectively. The ED-qBIC and MD-qBIC have different coupling efficiencies with respect to the incident beam polarization. For the lowest-order quasi-BICs, simulated electric field profiles resemble those of out-of-plane dipole modes (see Fig. 1D, insets, and fig. S1).

By tuning the period of the array and the proportions of the resonators, the central wavelengths of the quasi-BIC resonances can be tuned over a wide range. For emission normal to the QOM, the Q-factor is the highest because most of the system symmetry is preserved. Off-normal excitation leads to coupling to free-space radiation, reducing the Q-factor of each quasi-BIC resonance and lowering the field enhancement (fig. S2). Thus, we should also expect the emitted SPDC photon pairs to

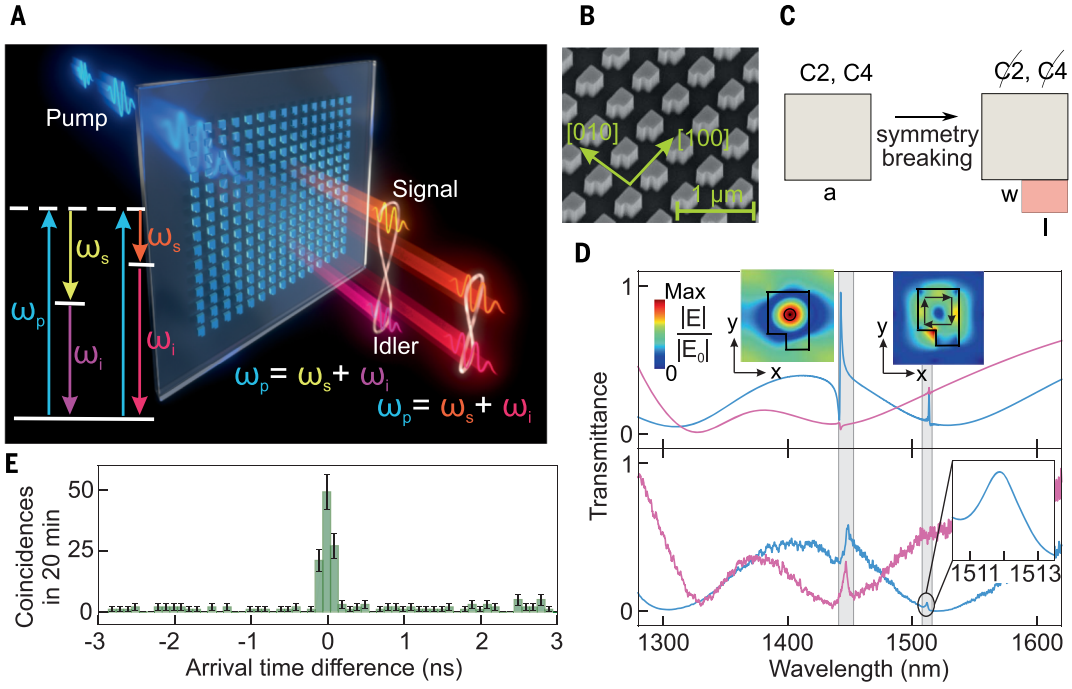

Fig. 1. Spontaneous parametric downconversion (SPDC) using symmetry-protected quasi-BIC resonances in a semiconductor metasurface. (**A**) Conceptual diagram of multiplexed entangled photon generation in a multiresonance semiconductor metasurface. (**B**) Scanning electron micrograph of the metasurface at an intermediate step of nanofabrication (see supplementary materials). (**C**) Structure of the broken-symmetry resonators (see table S1 for the various metasurfaces' dimensions). The addition of a small rectangle (pink) breaks the rotational symmetries C_2, C_4 of the metasurface, turning the BIC into a quasi-BIC. (**D**) Simulated (top) and measured (bottom) white-light linear transmission spectra of one QOM, for the incident polarization along the [110] crystal direction (magenta) and orthogonal to it (blue). Gray areas highlight the locations of the quasi-BIC resonances: ED-qBIC (λ = 1446.9 nm) and MD-qBIC (λ = 1511.8 nm). The insets show the normalized distribution and direction (black arrows) of electric field *xy* calculated at the center of the nanoresonator for both resonances. (**E**) Typical distribution of the photon arrival time difference for two detectors, demonstrating photon pair generation. Error bars denote the statistical uncertainty.

be radiated almost unidirectionally along the metasurface normal, as observed for emission from quantum dots embedded inside a symmetry-protected, quasi-BIC metasurface (*17*).

To demonstrate multiplexed entangled photon generation via SPDC, we investigated three QOMs, labeled QOM-A, QOM-B, and QOM-C, with different resonator sizes and spacings, such that the ED-qBIC and MD-qBIC optical modes were resonant at different wavelengths (Fig. 2, A to C, upper panels; also see table S1 and fig. S3). All metasurfaces were pumped with linearly polarized continuous-wave lasers of different wavelengths, focused into 140-μm spots. Two superconducting nanowire single-photon detectors placed at the two outputs of a fiber beamsplitter (fig. S4) enabled registration of photon pairs as joint detection events. For all QOMs considered, we registered a high number of simultaneous photon detections—coincidences (Fig. 1E)—which indicates the presence of photon pairs. For further details, see the supplementary materials. Figures S5 and S6 also show the results of second-harmonic generation, which is mediated by the same nonlinear tensor as SPDC and was therefore helpful for optimizing the experiment.

We then performed fiber-assisted spectroscopy of photon pairs with 3-nm resolution (see supplementary materials). The three corresponding SPDC spectra are shown in Fig. 2, A to C (bottom panels), each one below its white-light transmission spectrum. Thanks to the relaxed momentum conservation, the pump wavelength λ_p can be arbitrary, and thus we use different pumps and different QOMs to demonstrate various types of photon pair generation.

For QOM-A, we used λ_p = 723.4 nm, such that the degenerate wavelength $2\lambda_p$ overlapped with the ED-qBIC resonance wavelength. In this case, both SPDC photons were emitted within a single narrow peak, centered at the resonance wavelength $2\lambda_p$ = 1446.8 nm (Fig. 2A). The full width at half maximum (FWHM) of 4.3 nm matched the linewidth of the ED-qBIC resonance. This corroborates previous observations on QOMs (*12*) that the presence of an optical resonance enhances the quantum vacuum field within the resonance's bandwidth.

However, very different spectra were obtained when we pumped QOM-B at 718.2 nm, such that the degenerate wavelength $2\lambda_p$ was off-resonance from the ED-qBIC modes. Now, we found that the SPDC spectrum exhibited two narrow peaks, one centered at the ED-qBIC peak wavelength (λ_s = 1390.9 nm) and the other at a wavelength λ_i = 1485 nm (Fig. 2B). Here, the ED-qBIC resonance enhances the vacuum field at the signal wavelength, forcing the QOM to emit a photon at this wavelength simultaneously with its partner at the idler wavelength, as dictated by energy conservation:

$$\lambda_i = \left(\frac{1}{\lambda_p} - \frac{1}{\lambda_s}\right)^{-1} \quad (1)$$

This indicates that narrowband, frequency-nondegenerate photon pairs (ubiquitous in photonic state engineering, i.e., for heralding) have been generated from a nanostructured photonic device such as a metasurface.

The spectrum of the entangled photons gets richer when both ED-qBIC and MD-qBIC resonances are active in SPDC (Fig. 2C). We achieved this by pumping our third metasurface QOM-C at 725.4 nm, with the pump radiation polarized at 175°, so that the MD-qBIC resonance was activated. We now observed four peaks, two of them corresponding to signal photons emitted at the ED-qBIC (1359.4 nm) and MD-qBIC (1429.4 nm) resonances, and the other two to their idler partners. We found that because the MD-qBIC resonance has a higher Q-factor than the ED-qBIC resonance, its emission FWHM is smaller, causing the signal and idler SPDC spectra to also be narrower. It might be possible to obtain higher rates (i.e., larger peak heights), but we note that the Q-factor of a resonance provides only the upper boundary for SPDC enhancement, which also depends on the vacuum field distribution in the nanoresonators and the nonlinear tensor symmetry and values.

We also found that our QOMs can produce degenerate and nondegenerate photon pairs over a broad spectral range without considerable reduction of efficiency (Fig. 2D). As a consequence of the high-Q resonances, the efficiency is at least three orders of magnitude

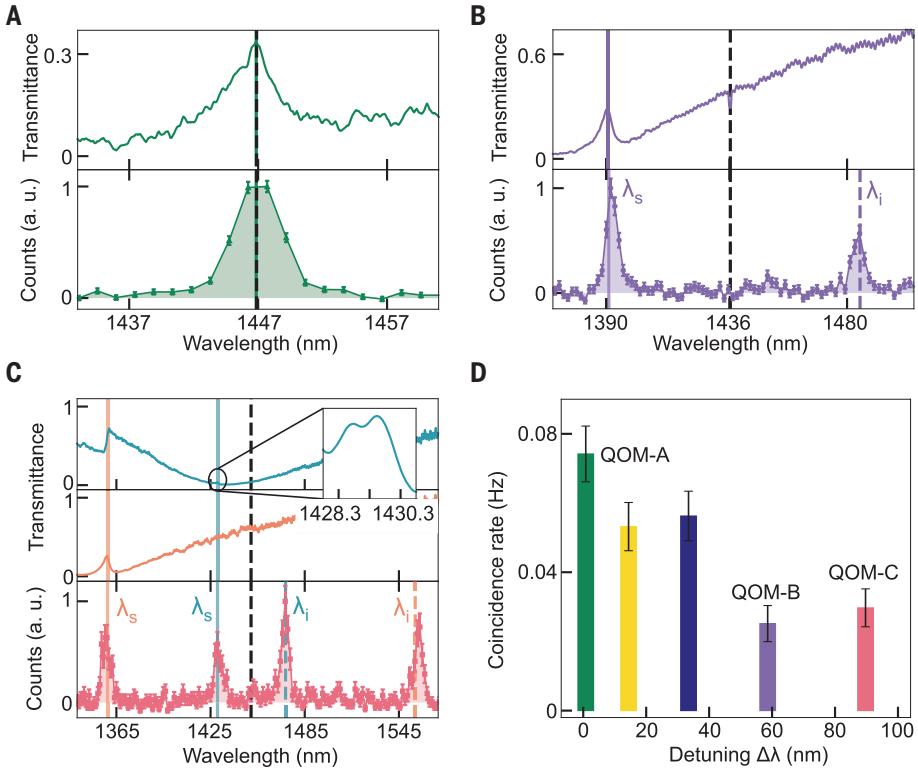

Fig. 2. SPDC spectra for the QOMs considered in this work. (**A** to **C**) Measured white-light transmission spectra (top) and SPDC spectra (bottom) for QOMs A, B, and C, respectively. The SPDC spectra show (A) degenerate photon pairs at wavelength $2\lambda_p$ = 1446.8 nm (vertical dashed line), which overlaps with the ED-qBIC resonance of QOM-A; (B) nondegenerate photon pairs, where only the signal photon is emitted at the ED-qBIC mode wavelength λ = 1390.9 nm (purple vertical solid line) of QOM-B; (C) two types of nondegenerate photon pairs, where signal photons are emitted at wavelengths λ = 1359.4 nm of the ED-qBIC resonance (orange vertical solid line) and λ = 1429.4 nm of the MD-qBIC resonance (green vertical solid line) of QOM-C. Both ED- and MD-qBIC modes are active in SPDC because of the choice of pump polarization. Black dashed lines show the degenerate wavelength $2\lambda_p$. The peak heights at signal and idler wavelengths are unequal because of the different detection efficiency of the two IR detectors and the asymmetric splitting ratio of the fiber splitter. (**D**) Coincidence rate, with 9.6 mW pumping at 725.4 nm, versus wavelength detuning $\Delta\lambda = 2\lambda_p - \lambda_{ED\text{-}qBIC}$ between the degenerate wavelength ($2\lambda_p$) and the ED-qBIC resonance, $\lambda_{ED\text{-}qBIC}$, of five different QOMs. Error bars denote the statistical uncertainty.

higher than in an unpatterned GaAs film of the same thickness (see supplementary text and fig. S7).

To verify the nonclassicality of our photon pairs, we measured the pump-power dependence of the second-order cross-correlation function (CF) at zero time delay, defined as $g^{(2)}_{si}(0) = \langle \hat{N}_s \hat{N}_i \rangle / \langle \hat{N}_s \rangle \langle \hat{N}_i \rangle$, where $\hat{N}_{s,i}$ are photon-number operators for the signal and idler modes. The cross-CF is measured as $g^{(2)}_{si}(0) = R_c/(R_s R_i T_c)$, where $R_{c,s,i}$ are the rates of the signal-idler coincidences, signal photon detections, and idler photon detections, respectively, and T_c is the coincidence resolution time (*27*). Because all three numbers $R_{c,s,i}$ scale linearly with the pump power, $g^{(2)}_{si}(0)$ has an inverse dependence on it, as indeed we observed (Fig. 3A). Although this dependence indicates photon pair detection, a formal proof of nonclassicality requires the violation of the Cauchy-Schwarz (CS) inequality (*28*),

$$\left[g^{(2)}_{si}(0)\right]^2 \le g^{(2)}_{ss}(0) \cdot g^{(2)}_{ii}(0) \qquad (2)$$

where $g^{(2)}_{ss,ii}(0)$ are second-order auto-CFs for signal and idler modes, respectively. For QOM-B, which generates signal and idler photons at two distinguishable wavelengths (1390.9 nm and 1485 nm), we measured the auto-CFs of modes s and i after 50-nm FWHM bandpass filters centered at 1400 nm (s) and 1475 nm (i), respectively (Fig. 3, B and C). Single-count graphs for each measurement are shown in fig. S9. We obtained $g^{(2)}_{ss}(0) = 1.6\pm0.3$ and $g^{(2)}_{ii}(0) = 1.2\pm0.2$. The cross-CF, measured without bandpass filters (Fig. 3D), was $g^{(2)}_{si}(0) = 10.5\pm1.1$. Hence, the CS inequality is violated by >50 standard deviations, $[g^{(2)}_{si}(0)]^2 = 110\pm2$, $g^{(2)}_{ss}(0) \cdot g^{(2)}_{ii}(0) = 1.9\pm0.3$, revealing the nonclassical character of photon pairs.

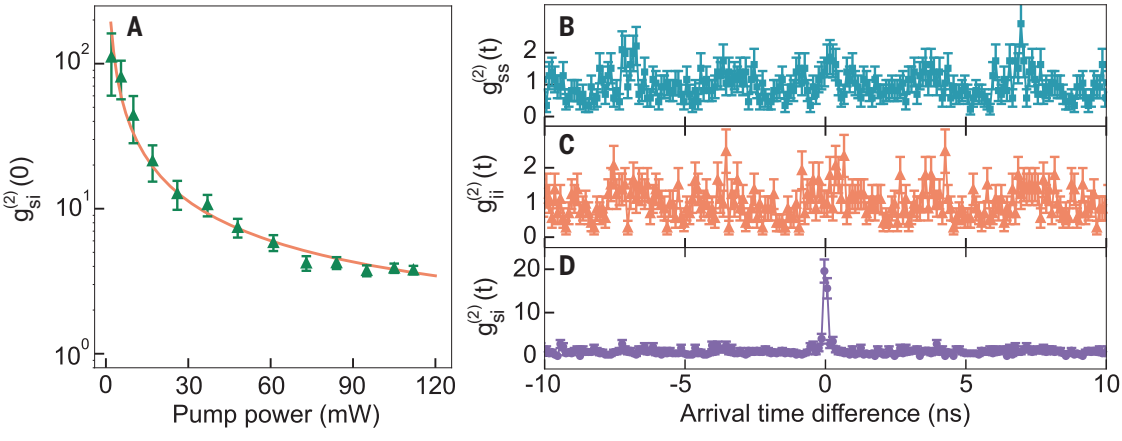

Fig. 3. Second-order cross-correlation and autocorrelation functions. (**A**) Pump-power dependence of the second-order cross-correlation function at zero time delay measured for photon pairs emitted by QOM-A (points) and its theoretical fit (line). For raw data, see fig. S8. (**B** and **C**) Second-order auto-correlation functions $g^{(2)}_{ss}$ and $g^{(2)}_{ii}$ measured for QOM-B at the signal (1390.9 nm) and idler (1485 nm) wavelengths, respectively. (**D**) Second-order cross-correlation function $g^{(2)}_{si}$ measured for QOM-B. Error bars are obtained from the statistical uncertainties via the propagation of errors.

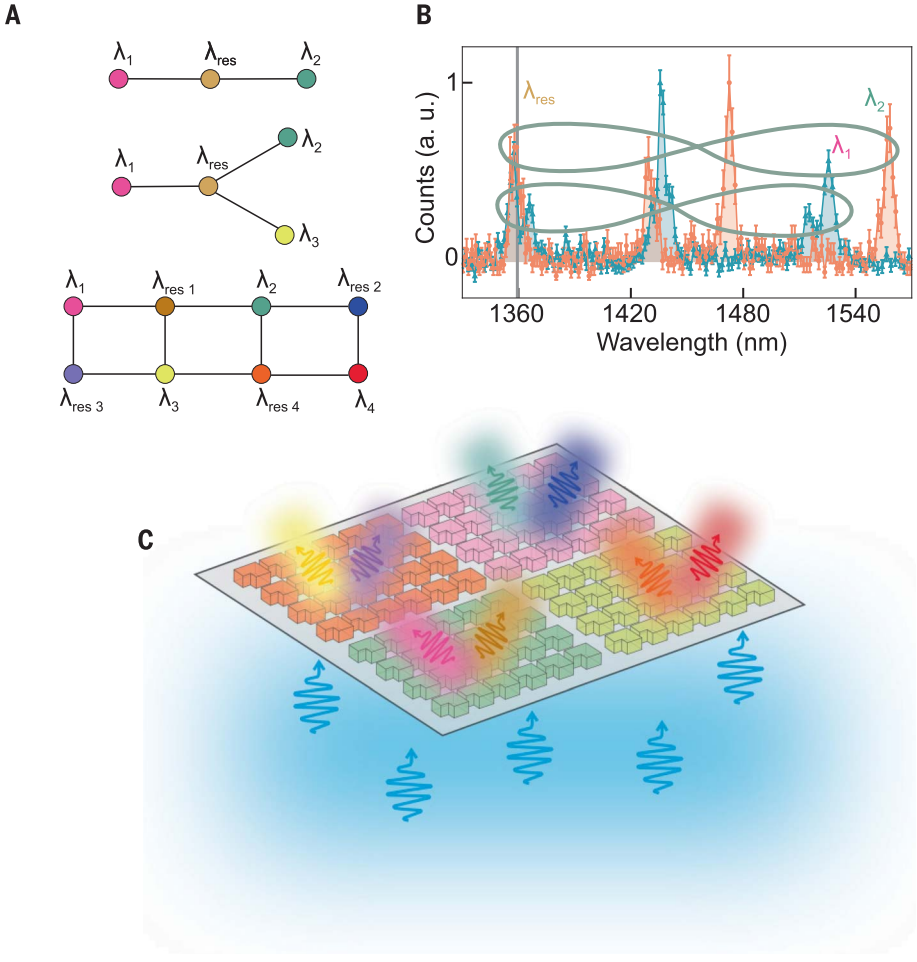

Fig. 4. Cluster state generation with QOMs. (**A**) Examples of cluster states: a linear three-qubit state (top), a Greenberger-Horne-Zeilinger state (middle), and a more general graph state (bottom). Links between the vertices are provided by different pumps. (**B**) SPDC spectrum illustrating how a linear three-qubit graph state of photons $|\lambda_{res}\rangle$, $|\lambda_1\rangle$, $|\lambda_2\rangle$ can be generated from QOM-C. (**C**) Spatial multiplexing of four metasurfaces for generating the state of (A), bottom, using a single multifrequency pump beam.

The presence of narrow optical resonances allows one to create, apart from entangled states, more complicated graph quantum states (Fig. 4A). In our setup (fig. S4), the state preparation relies on the fiber beamsplitter sending a photon to each detector; events where both photons arrive at the same detector are ignored. For a nondegenerate photon pair at wavelengths λ_{res} (resonant) and λ_1 (matching via energy conservation), after the beamsplitter, photon $|\lambda_{res}\rangle$ is path-entangled with photon $|\lambda_1\rangle$. For a second nondegenerate pair at wavelengths λ_{res} and λ_2, photon $|\lambda_{res}\rangle$ is also path-entangled with photon $|\lambda_2\rangle$ after the beamsplitter. Note that this photon pair needs another pump for its generation. If photons $|\lambda_{res}\rangle$ from each pair are indistinguishable, which requires two mutually coherent pumps, a linear graph state of three pairwise entangled qubits is created (Fig. 4A, top). This strategy for cluster state generation, called pairwise coupling (*6*), can be implemented using pump beams at wavelengths of 725.4 nm and 718.2 nm and an ED-qBIC resonance at λ_{res} = 1359.4 nm. Figure 4B shows the corresponding spectra with orange and blue colors, respectively, with only two entangled photon pairs ($|\lambda_{res}\rangle$ and $|\lambda_1\rangle$, $|\lambda_{res}\rangle$ and $|\lambda_2\rangle$) marked for simplicity. In our experiment, the pump beams are incoherent, but they still provide the desired spectrum. By adding a third pump, generating photon pairs at wavelengths λ_{res} and λ_3, a more complicated graph state can be created, called a Greenberger-Horne-Zeilinger state (*5*) (Fig. 4A, middle).

The state becomes increasingly complex by adding multiple coherent pump beams at different wavelengths—that is, using a frequency comb or a filtered supercontinuum as an excitation source. By appropriately matching the wavelength separation of the comb and the optical resonances of the QOMs, photons at multiple wavelengths can be entangled via pairwise couplings. With this approach, one could implement a scalable cluster state, needed for one-way quantum computation (*5*), as shown in Fig. 4A (bottom). Such methods of quantum state engineering are enabled by the use of our QOMs with relaxed phase matching and engineered high-Q resonances, and are impossible with bulk crystal or waveguide SPDC sources. Moreover, QOMs provide a unique way to spatially multiplex multiple metasurfaces within the area of a single pump beam (possibly multifrequency) by exciting resonances at different wavelengths and entangling multiple photon pairs across separate wavelengths with a single multifrequency pump beam, as shown in Fig. 4C. But even without links between different pairs, the existence of multifrequency or multispatial channels suggests a new architecture for heralding single photons in many different modes (*29*).

The use of a highly nonlinear metasurface with narrowband resonances at arbitrary, discrete, and multiple wavelengths enables new opportunities for generating quantum states that have no counterpart when using traditional nonlinear optical crystals or passive (*30*) or conventional Mie-type metasurfaces (*12*). First, we have shown enhancement in pair emission rates of at least three orders of magnitude relative to an unpatterned film of the same material and thickness. Second, we have demonstrated nonclassical correlations between downconverted photons at broadly separated wavelengths, opening the possibility of photon heralding. Third, combining single or multiple coherent laser sources with two or more quasi-BIC resonances from a single or multi-patch metasurface, we can create photon pairs at multiple frequencies with comparable efficiencies. Such a multitude of photon pairs can be used to create complex photon quantum states, including cluster states and multichannel single photons, that could facilitate compact quantum information processing (*4*, *5*, *29*). Finally, achieving this level of quantum state engineering with a single nanoscale source can potentially lead to future miniaturization of photonic quantum processing, not possible today with other photonic platforms.

REFERENCES AND NOTES

1. B. Lounis, M. Orrit, *Rep. Prog. Phys.* **68**, 1129–1179 (2005).
2. M. Chekhova, *Prog. Optics* **56**, 187–226 (2011).
3. R. Schnabel, *Phys. Rep.* **684**, 1–51 (2017).
4. G. Vallone, E. Pomarico, P. Mataloni, F. De Martini, V. Berardi, *Phys. Rev. Lett.* **98**, 180502 (2007).
5. H. J. Briegel, D. E. Browne, W. Dür, R. Raussendorf, M. van den Nest, *Nat. Phys.* **5**, 19–26 (2009).
6. M. V. Larsen, X. Guo, C. R. Breum, J. S. Neergaard-Nielsen, U. L. Andersen, *Science* **366**, 369–372 (2019).
7. G. Li, S. Zhang, T. Zentgraf, *Nat. Rev. Mater.* **2**, 17010 (2017).
8. A. Krasnok, A. Alù, *ACS Photonics* **9**, 2–24 (2022).
9. M. Shcherbakov, S. Liu, I. Brener, A. Fedyanin, in *Dielectric Metamaterials*, I. Brener, S. Liu, I. Staude, J. Valentine, C. Holloway, Eds. (Elsevier, 2020), pp. 223–248.

10. A. S. Solntsev, G. S. Agarwal, Y. S. Kivshar, *Nat. Photonics* **15**, 327–336 (2021).
11. J. Liu *et al*., *Opto-Electron. Adv.* **4**, 200092 (2021).
12. T. Santiago-Cruz *et al*., *Nano Lett.* **21**, 4423–4429 (2021).
13. L. Li *et al*., *Science* **368**, 1487–1490 (2020).
14. J. Zhang *et al*., *Sci. Adv.* **8**, eabq4240 (2022).
15. C. Okoth, A. Cavanna, T. Santiago-Cruz, M. V. Chekhova, *Phys. Rev. Lett.* **123**, 263602 (2019).
16. S. Liu *et al*., *Nat. Commun.* **9**, 2507 (2018).
17. S. Liu *et al*., *Nano Lett.* **18**, 6906–6914 (2018).
18. P. P. Vabishchevich *et al*., *ACS Photonics* **5**, 1685–1690 (2018).
19. K. Koshelev, S. Lepeshov, M. Liu, A. Bogdanov, Y. Kivshar, *Phys. Rev. Lett.* **121**, 193903 (2018).
20. C. W. Hsu, B. Zhen, A. D. Stone, J. D. Joannopoulos, M. Soljacic, *Nat. Rev. Mater.* **1**, 16048 (2016).
21. T. Santiago-Cruz, V. Sultanov, H. Zhang, L. A. Krivitsky, M. V. Chekhova, *Opt. Lett.* **46**, 653–656 (2021).
22. C. Okoth *et al*., *Phys. Rev. A* **101**, 011801 (2020).
23. G. Marino *et al*., *Optica* **6**, 1416 (2019).
24. S. D. Gennaro *et al*., *ACS Photonics* **9**, 1026–1032 (2022).
25. S. Campione *et al*., *ACS Photonics* **3**, 2362–2367 (2016).
26. A. Cerjan *et al*., *Sci. Adv.* **7**, eabk1117 (2021).
27. L. Mandel, E. Wolf, *Optical Coherence and Quantum Optics* (Cambridge Univ. Press, 1995).
28. D. F. Walls, G. J. Milburn, *Quantum Optics* (Springer, 2008).
29. A. Crespi *et al*., *Nat. Photonics* **7**, 545–549 (2013).
30. K. Wang *et al*., *Science* **361**, 1104–1108 (2018).

ACKNOWLEDGMENTS

We thank P. Vabishchevich, A. V. Rasputnyi, V. Sultanov, and M. Poloczek for their help at the initial stage of the experiment, and M. Lippl and N. Y. Joly for giving us access to the tunable continuous-wave laser. **Funding:** T.S.-C. and M.V.C. are part of the Max Planck School of Photonics, supported by the Bundesministerium für Bildung und Forschung, the Max Planck Society, and the Fraunhofer Society. M.V.C. acknowledges support by the Deutsche Forschungsgemeinschaft, Project ID 429529648, TRR 306 QuCoLiMa ("Quantum Cooperativity of Light and Matter"). S.D.G., O.M., and I.B. were supported by the US Department of Energy, Office of Basic Energy Sciences, Division of Materials Sciences and Engineering (grant BES 20-017574). The work was performed, in part, at the Center for Integrated Nanotechnologies, an Office of Science User Facility operated for the US Department of Energy, Office of Science. Sandia National Laboratories is a multi-mission laboratory managed and operated by National Technology and Engineering Solutions of Sandia LLC, a wholly owned subsidiary of Honeywell International Inc., for the US Department of Energy's National Nuclear Security Administration under contract DE-NA0003525. This paper describes objective technical results and analysis. Any subjective views or opinions that might be expressed in the paper do not necessarily represent the views of the US Department of Energy or the United States government. **Author contributions:** Conceptualization, T.S.-C., S.D.G., I.B., M.V.C.; methodology, T.S.-C., S.D.G., O.M., S.A., J.R., I.B., M.V.C.; investigation, T.S.-C., S.D.G.; visualization, T.S.-C., S.D.G., I.B., M.V.C.; funding acquisition, I.B., M.V.C.; project administration, I.B., M.V.C.; supervision, I.B., M.V.C.; writing–original draft, T.S.-C., S.D.G.; writing–review and editing, T.S.-C., S.D.G., I.B., M.V.C. **Competing interests:** The authors declare no competing interests. **Data and materials availability:** All data needed to evaluate the conclusions in this paper are available in the manuscript or the supplementary materials.

SUPPLEMENTARY MATERIALS

science.org/doi/10.1126/science.abq8684
Materials and Methods
Supplementary Text
Figs. S1 to S10
Tables S1 and S2
References (*31*–*34*)

Submitted 5 May 2022; accepted 21 July 2022
10.1126/science.abq8684